CHINESE OPTICS LETTERS

Vol. 23, No. 1 | January 2025

Angular-adaptive spin-locked retroreflectors based on reconfigurable origami two-dimensional metagrating

Zhibiao Zhu (朱志标), Yongfeng Li (李勇峰)*, Zhe Qin (秦 哲), Lixin Jiang (蒋李鑫), Wenjie Wang (王雯洁), Hongya Chen (陈红雅), Jiafu Wang (王甲富), Lin Zheng (郑 麟), and Shaobo Qu (屈绍波)

Shaanxi Key Laboratory of Artificially-Structured Functional Materials and Devices, Air Force Engineering University, Xi'an 710051, China

*Corresponding author: liyf217130@126.com

Received June 12, 2024 | Accepted July 29, 2024 | Posted Online February 14, 2025

The retroreflector based on a gradient metasurface can reflect electromagnetic (EM) waves to the source, and it is small in size and lightweight. However, even if the previous retroreflectors can be used for angle adaptation, the working efficiency declines sharply at large angles. In this paper, a retroreflector is designed based on a reconfigurable origami two-dimensional (2D) metagrating for efficient spin-locked retroreflection and for suppressing unwanted Floquet diffraction channels. After the retroreflection, the handedness of the wave remains consistent with the incident. By changing the folding state of the origami metagrating, the adaptive tangential momentum can be transferred to the incident wave, providing high-performance retroreflection over a continuous incidence angle range of 30°–45.8° (*x*-direction) and 30°–81° (*y*-direction). As proof of concept, an electric metagrating-based retroreflector is fabricated in the microwave frequency band, and the simulation and experimental results are consistent. This adaptive origami spin-locked metasurface has promising applications in spin-optics devices, communication systems, remote sensing, and radar cross-section (RCS) enhancement.

Keywords: origami; retroreflector; metagrating.
DOI: 10.3788/COL202523.010501

1. Introduction

Retroreflection is defined as the reflection of a portion of the incident electromagnetic (EM) wave energy on the illuminated device or surface back to the incident direction. In the microwave region, scientists maximize backscatter, which has applications in communications and stealth. Retroreflectors are extremely important in laser tracking and optical systems in the optical domain. Conventional retroreflectors include corner reflectors, Luneburg lenses, planar retrodirective antenna arrays, and cat-eye reflectors[1–6]. More design ideas have been proposed as metasurfaces are introduced to design retroreflective devices. The cascaded metasurface achieves broadband retroreflection with the help of the stacking of the double-layer structure[7–9]. Subsequently, gradient metasurface retroreflectors are proposed[10,11]. The phase gradient metasurface can only reflect a specific circular-polarized incident photon to one particular incident angle ($+\theta_{RT}$). The other orthogonal circular-polarized incident photon can only be incident in another direction ($-\theta_{RT}$) to realize the retroreflection, where θ_{RT} represents the angle of the retroreflection. Two intelligent adjustable phase gradient metasurfaces have been proposed to implement retroreflectors. They cannot solve the abovementioned problems and can only realize the retroreflection adjustable of circularly polarized (CP) photons in one direction[11].

In addition, recent research[12–17] has pointed out that retroreflection efficiency based on a gradient metasurface design drops sharply in the case of large incidence angles. The fundamental reason is that the method does not consider impedance matching under a large angular incidence, which leads to parasitic reflection or energy loss in the undesirable direction of the retroreflector[12]. The proposal of metagrating solves part of the problem[18]. After designing a carefully customized bianisotropic particle, the periodic array regulates arbitrary wavefront transformations with uniform efficiency. The metagrating avoids the discretization of the continuous phase or impedance curve. The scatterer can be designed to suppress unwanted diffraction orders and redirect the incident power to the desired diffraction order with unit efficiency. However, to achieve spin-locked retroreflection, the metagrating cannot be one-dimensional (1D). The reason is that the 1D metagrating is sensitive to the polarization of the incident wave. The spin of the light refers to the right- and left-handed circularly polarized (RCP and LCP) lights, and the spin direction of the orthogonal CP light is precisely the opposite. As a frontier research field of spin optics, metasurfaces based on CP modulation have received extensive attention[19–21].

Here, we propose a two-dimensional (2D) metagrating based on Miura origami to achieve spin-locked retroreflection over a

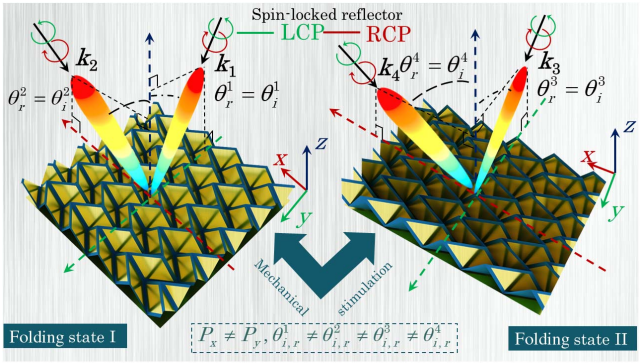

Fig. 1. The proposed spin-locked retroreflector based on the Miura origami metagrating design. The origami metagrating is 2D. Therefore, the retroreflection can be achieved in both the x and y directions. When the origami metagratings are in different folding states, $P_x \neq P_y$, $\theta_{i,r}^{1} \neq \theta_{i,r}^{2} \neq \theta_{i,r}^{3} \neq \theta_{i,r}^{4}$.

range of continuous incidence angles. When the oblique incident EM wave vector is along the x- or y-direction, the origami 2D metagrating can suppress the unwanted diffraction orders and reroute the incident EM energy in the desired direction. The reflection amplitude is consistent under the orthogonal linear polarization incidence $[\theta_{\text{in}} = \lambda/(2^{*}p)]$. θ_{in} is the incident angle of the EM wave. According to $E_{\text{LCP}} = E_x + iE_y$ and $E_{\text{RCP}} = E_x - iE_y$, the handedness of the reflected EM wave does not change when the CP wave is incident (Fig. 1). 2D origami metagratings can change the folding state continuously, so the incident photons acquire adaptive tangential momentum. Therefore, high-performance retroreflectors can be achieved. In contrast to the above methods, the origami 2D metagrating implements an angle-adapted spin-locked retroreflector. It is worth mentioning that the proposed structure will reflect the orthogonal spin photons in one direction instead of two directions.

2. Principle and Unit Cell Design

We design 2D metagratings in a single unit cell based on previous studies to generate the desired spin-locked retroreflection. The 2D metagratings can be realized by loading metal patches on the four faces of a Miura origami with the same shape as the faces. The linearly polarized wave incident from the x- or y-direction can excite electric dipoles on the metallic patch, which is the primary physical mechanism behind our proposed metagrating. The origami is a reconfigurable structure, when the unit length in the x- or y-direction is changed, the angle of the retroreflection changes. The origami 2D metagratings (of appropriate size) comprise subwavelength periodic arrays that redirect the obliquely incident waves to the desired reflection direction with near-uniform efficiency. According to the basic design theory of metagrating, when the period is set, the direction of the flip wave vector can be aligned with the direction of the Floquet mode propagation. When the oblique incident direction (wave vector direction) is along the x-axis, the Floquet propagation mode is $(\pm n)0$. Conversely, when the oblique incident direction is along the y-axis, the Floquet propagation mode is $0(\pm m)$. If the wave vector direction is along the y-axis, then we choose to align the $0(-1)$ Floquet mode with the desired reflection direction, (i.e., $\theta_{0(-1)} = \theta_{\text{Ref}}$). θ_{Ref} is the reflection angle of the EM wave. The period y_p of the 2D grating along the y-direction can be represented by the wavelength λ_y, the Floquet modulus angle $\theta_{0(-1)}$ of $0(-1)$, and the incidence angle as follows:

$$y_p = \frac{\lambda_y}{\sin\theta_{\text{in}}^{y} - \sin\theta_{0(-1)}}. \tag{1}$$

When the wave vector direction is along the x-direction, the period x_p of the 2D grating along the x-axis can be expressed by the wavelength λ_x, the Floquet modulus angle $\theta_{(-1)0}$ of $(-1)0$, and the incidence angle as follows:

$$x_p = \frac{\lambda_x}{\sin\theta_{\text{in}}^{x} - \sin\theta_{(-1)0}}. \tag{2}$$

First, we analyze the case when the wave vector direction is along the x-axis, and the analysis is similar for the y-axis. When the wave vector is along the x-direction, all propagating Floquet mode fields outside the $(-1)0$ mode need to be eliminated. In principle, it can be any higher-order mode (i.e., $n0$ mode of $|n| > 2$) on the reflection direction. However, this would make the elimination of unwanted Floquet channels more challenging because there are more of them. Thus, we establish that 00, 10, and $(-1)0$ are the unique propagating Floquet modes, which implies $|k_{y(\pm 2)0}| > k_0$. As a result, the following restrictions can be obtained:

$$\begin{cases} \theta_{(-1)0} < \arcsin\left(2\sin\theta_{\text{in}}^{y} - 1\right), & \text{for } 0 < \theta_{\text{in}}^{y} < \arcsin\left(\frac{1}{3}\right) \\ \theta_{(-1)0} < \arcsin\left(2\sin\theta_{\text{in}}^{y} - \frac{1}{2}\right), & \text{for } \arcsin\left(\frac{1}{3}\right) < \theta_{\text{in}}^{y} < \frac{\pi}{2} \end{cases}. \tag{3}$$

Combining this condition with Eq. (1) yields $\theta_{(-1)0} < -30°$, which means that we should not choose a reflection angle with an absolute value of less than 30°. After setting the period, we designed the block scatterer to support nulls in the direction of all open Floquet channels except for the $(-1)0$ channel. In order to achieve the retroreflection of the CP waves with spin-locked, both transverse magnetic (TM) and transverse electric (TE) polarized waves must be considered. When the wave-vector is along the x-axis, Fig. 2(a) shows a schematic of a general spin-locked metagrating with TE polarization under three open Floquet channels. The proposed metagrating consists of four electric dipoles, which can completely transfer the TE polarized wave to the $\text{TE}_{(-1)0}$ Floquet mode. Similarly, when a TM-polarized incident wave illuminates the structure, its expected Floquet mode is $\text{TM}_{(-1)0}$. Therefore, the metagrating can steer the incident wave in the anomalous direction (retroreflection). To clarify the spin-locking properties of CP waves, we assume that

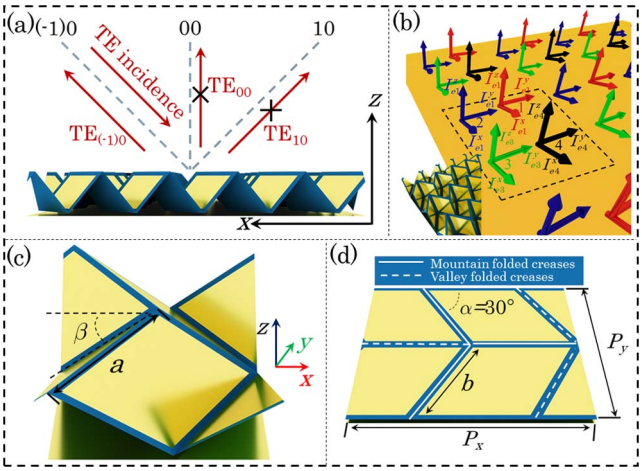

Fig. 2. (a) Schematic representation of a general spin-locked metagrating with three Floquet modes under a TE-polarized incidence. It is worth mentioning that this principle also applies to a TM-polarized incidence. (b) Demonstration of induced electric current on the ground plane. (c) Schematic diagram of the folded Miura origami unit cell. The substrate of the Miura origami is a polyimide material, which is located on a perfect electrical conductor. The thickness of the substrate is only 0.075 mm, and the dielectric constant is ε_r = 3. (d) The distribution of creases. The period of the structure in the *x*-axis is P_x, and the period in the *y*-axis is P_y.

A_1 and A_2 are the amplitudes of the incident co-polarized reflections from TE and TM polarization, respectively. In order to achieve spin-locked retroreflection, the co-polarized amplitudes of the TE and TM modes must be the same, i.e., $A_1 = A_2$.

As shown in Fig. 2(b), the red, blue, green, and black arrows indicate the electric currents of the first, second, third, and fourth dipoles in a single unit cell, respectively. The symbol $I_{ei}^{x,y,z}$ represents the electric current component on the ith ($i = 1, 2, 3, 4$) dipoles. When the wave vector is along the x-axis, the periodicity of this direction is designed to preserve only the $(-1)0$ propagating Floquet mode. Since the EM energy is concentrated in the x–z plane, no radiation exists in the y–z plane. We assume that the TE plane wave illuminates the origami retroreflector, that is, $E_{\text{in}} = E_0(x \cos\theta_{\text{in}} + z \sin\theta_{\text{in}})$ $\exp(ik_0 \sin\theta_{\text{in}} x - ik_0 \cos\theta_{\text{in}} z)$, where E_0 is its amplitude, k_0 is the wavenumber in free space, and θ_{in} is the incidence angle defined counterclockwise to the z-axis. According to the Floquet mode analysis[22], the radiation field of the $n0$ Floquet mode is the TE wave, and the total scattered field of the array can be expressed by the Floquet mode,

$$E_{n0} = y(\Phi_{n0}^1 + \Phi_{n0}^2 + \Phi_{n0}^3 + \Phi_{n0}^4)\exp(ik_{xn0}x + ik_{zn0}z), \quad (4)$$

where the term Φ_{n0}^i is the expression related to electric currents on the ith dipoles. For the $n0$ Floquet mode, $k_{xn0} = k_{x0} + \frac{2n\pi}{b} = k_0 \sin\theta_{n0}$ is the wavenumber in the x-direction, and $k_{zn0} = \sqrt{k_0^2 - k_{xn0}^2} = k_0 \cos\theta_{n0}$ is the wavenumber in the z-axis. Where $(i = 1, 2, 3, 4)$ is the expression related to the current on the ith dipole, the distance between the dipoles, and the lattice constant of the Miura origami. The parameter b is the period of the structure in the x-axis. Assuming that an oblique incident TE wave propagating in the z–x plane illuminates the origami retroreflector, the electric field of the directly reflected wave from the ground plane is expressed as

$$\boldsymbol{E}_r = \mathbf{y}E_0 \exp(ik_{x00}x + ik_{z00}z). \quad (5)$$

Direct reflection in the ground plane can cancel the co-polarized wave energy in the specular direction. Therefore, we can obtain the following conditions (these relations hold for both TM and TE polarized incidences),

$$\begin{cases} \Phi_{00}^1 + \Phi_{00}^2 + \Phi_{00}^3 + \Phi_{00}^4 = 0 \\ \Phi_{10}^1 + \Phi_{10}^2 + \Phi_{10}^3 + \Phi_{10}^4 + E_0 = 0 \end{cases}. \quad (6)$$

Equation (6) is similar to the equation in Ref. [23]. Moreover, the analysis is identical to that in the x-axis when the wave vector is incident along the y-axis. When the folding state of Miura origami changes, the x- and y-axis periods change continuously, which is the key to realizing the dynamic adjustment of the retroreflection angle.

We implement a spin-locked retroreflection based on a Miura origami 2D metagrating to achieve the above configuration. As shown in Fig. 2(c), we adopt a control variable β to control the folding state of the origami. In Miura origami, the face is a diamond, and the side length is a. We redefine the simulation structure. Unit cell boundaries are set in the x- and y-directions, and open added space is set in the z-direction. The specific simulation setup can be referred to in the previous work[24]. Figure 2(d) shows the acute angle of the face $\alpha = 30°$. There are diamond-shaped metallic patches of the same shape as the origami facets on the origami surface, with sides of length b on both sides. The period of the origami in the x- and y-directions can be expressed by the following relations:

$$\begin{cases} P_y = 2a\cos\delta \\ P_x = 2a(\sin\delta\cos\alpha + \cos\delta\cos\beta\sin\alpha) \\ \delta = \tan^{-1}\left[\frac{1}{\tan\alpha\cos\beta}\right] \end{cases}. \quad (7)$$

After the periods in the x- and y-direction have been determined, the following conditions must be satisfied to achieve an adaptive retroreflection metagrating,

$$\begin{cases} -\theta_{\text{ref}}^x = \theta_{\text{in}}^x = \arcsin\left(\frac{\lambda}{2P_x}\right) \\ -\theta_{\text{ref}}^y = \theta_{\text{in}}^y = \arcsin\left(\frac{\lambda}{2P_y}\right) \end{cases}, \quad (8)$$

where $\theta_{\text{ref}}^{x,y}$ is the retroreflection angle whose absolute value equals the incidence angle $\theta_{\text{in}}^{x,y}$. λ is the EM wave wavelength.

3. Results and Discussion

We employ the time domain solver in the CST commercial simulation software to simulate far-field scattering from three first-

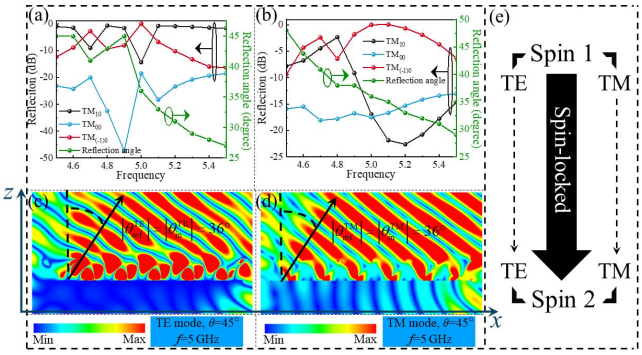

Fig. 3. Reflection coefficients and angles versus frequency for different Floquet modes under (a) the TE- and (b) the TM-polarized incidences. When the folding angle β of the retroreflector is tuned to 45°, the corresponding scattered electric field distribution of (c) the TE- and (d) the TM-polarized incidences on the *zOx* plane is obtained at $\theta_{in} = 36°$ illumination angle. (e) Schematic diagram of spin-locked retroreflection.

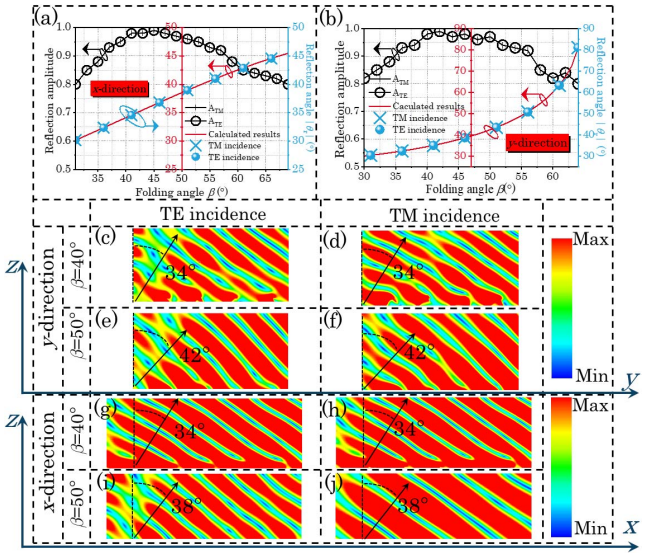

Fig. 4. Simulation results of retroreflection amplitude and angle as a function of fold angle β under the TE- and TM-polarized incidences: (a) *x*-direction and (b) *y*-direction. The corresponding scattered electric field distribution of the TE- and TM-polarized incidences on the *zOx* plane: (c)–(d) $\theta_{in} = 34°$, $\beta = 40°$ and (e)–(f) $\theta_{in} = 42°$, $\beta = 50°$. The corresponding scattered electric field distribution of the TE- and TM-polarized incidences on the *zOy* plane: (g)–(h) $\theta_{in} = 34°$, $\beta = 40°$ and (i)–(j) $\theta_{in} = 38°$, $\beta = 50°$.

order Floquet modes. Figures 3(a) and 3(b) show the reflectance (normalized) and reflection angle versus frequency for the three Floquet modes with the folding angle tuned to 45° under the TE- and TM-polarized incidences, showing a moderately wide response in terms of frequency. The calculated $|\theta_{ref}^{TE}| = |\theta_{in}^{TE}| = 36°$ under Eq. (3) limits the total power of the EM wave energy of the other high-order Floquet modes and is almost suppressed to zero. At the design frequency of 5 GHz, the energy of the oblique incident EM wave is redirected to the required Floquet mode as expected, namely $TE_{(-1)0}$ for the TE-polarized incidence and $TM_{(-1)0}$ for the TM-polarized incidence. The reflected EM waves of the TE- and TM-polarized incidences have the same amplitude and propagate along the same path, verifying that the proposed origami metagrating can achieve spin-locked retroreflection. Figures 3(c) and 3(d) show the scattered electric field distribution in the *zOx* plane for the incidence angle at $\theta_{in} = 36°$ under TE- and TM- polarization incidences, respectively. Both the TE- and TM-polarized incidences achieve retroreflection. The basic principle of spin-locked retroreflection is further revealed in Fig. 3(e), where we consider the CP wave as a superposition of TE-and TM-polarized incidences.

The performance of the angle adaptive retroreflection is shown in Fig. 4. If the wave vector is along the *x*-axis at 5 GHz ($\lambda = 60$ mm), then by adjusting the folding angle of 31° to 70°, the spin-locked retroreflection can be achieved in the continuous incidence angle range of 30.2° to 45.8°. The corresponding periodic variation along the *x*-direction is 59.7 to 41.9 mm. If the wave vector is along the *y*-direction, when $f = 5$ GHz, by adjusting the folding angle of 30° to 64°, the spin-locked retroreflection in the continuous incidence angle range of 30° to 81° can be achieved. The corresponding periodic variation along the *y*-direction is 60 to 30 mm. Figures 4(a) and 4(b) show the simulated co-polarized retroreflection amplitude plots versus the folding angle under the TE- and TM-polarized incidences. Figure 4(a) shows the *x*-direction, and Fig. 4(b) shows the *y*-direction. The retroreflection amplitudes of the TE- and TM-polarized incidences are approximately the same. This property verifies that the origami 2D metagrating can reflect CP waves in the continuous incident angle range of 30.2°–45.8° (*x*-direction) and 30°–81° (*y*-direction) and can well maintain the spin state of the EM waves. The reflection amplitude is calculated as follows: the scattering intensity is normalized to the specular reflection intensity at the corresponding incidence angle for perfect electrical conductors of the same size. Since the incident angle conforms to the restriction of Eq. (3), the EM wave propagates mainly on the first-order Floquet channel. According to Eqs. (7) and (8), the relationship curve between the retroreflection angle and the folding angle can be calculated. As shown in Figs. 4(a) and 4(b), when the wave vector is incident along the *x*- or *y*-direction, the simulated retroreflection angle changes with the folding angle under the TM- and TE-polarized incidences, which conforms to the above curve law. When the wave vector is along the *y*-direction, Figs. 4(c)–4(f) show the electric field profiles for the TE and TM modes at incidence angles of 34° and 42°, corresponding to the folding angles of 40° and 50°, respectively. When the wave vector is incident along the *x*-direction, Figs. 4(g)–4(j) show the electric field profiles for the TE and TM modes at incidence angles of 34° and 38°, corresponding to the folding angles of 40° and 50°, respectively.

In order to explore the distribution of the EM wave energy on different Floquet channels, we need to simulate the electric field behavior of the origami metagrating in the far field. Figure 5 shows the simulation results of the far-field scattering intensity distribution of the retroreflection at different incidence angles

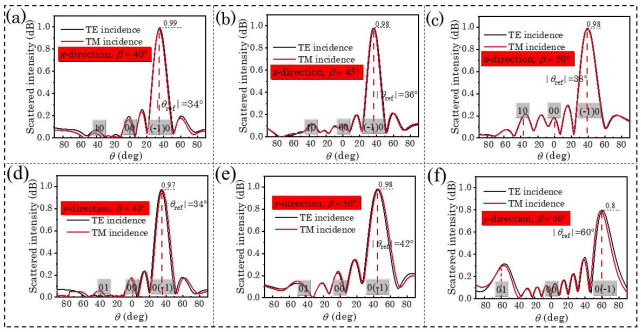

Fig. 5. Relationship between the scattering intensity and θ under TE- and TM-polarization incidences. *x*-direction: (a) $\beta = 40°$, $|\theta_{ref}| = 34°$, (b) $\beta = 45°$, $|\theta_{ref}| = 36°$, and (c) $\beta = 50°$, $|\theta_{ref}| = 38°$. *y*-direction: (d) $\beta = 40°$, $|\theta_{ref}| = 34°$, (e) $\beta = 50°$, $|\theta_{ref}| = 42°$, and (f) $\beta = 60°$, $|\theta_{ref}| = 60°$.

for the TE- and TM-polarization incidences. At different folding angles, the scattering intensity is normalized to the specular reflection intensity at the corresponding incidence angle for an ideal conductor of the same size. When the EM wave is incident along the *x*-direction and the folding angle changes from 40° to 50°, the energy of the reflected EM wave is mainly concentrated in the (−1)0 channel. The EM wave energies of 10 and 00 are effectively suppressed in all three folding states. The EM wave energy exists on other higher-order Floquet channels. However, these energies are insignificant compared to the energy of the wave in the (−1)0 channel. When the EM wave is incident along the *y*-direction, the reflected energy is mainly concentrated in the 0(−1) channel.

Using two double-ridge horn antennas (2–6 GHz) connected to a vector network analyzer, the spin-locked retroreflection based on origami metagrating is experimentally verified in an anechoic chamber. An origami spin-locked retroreflector consisting of 6×6 unit cells is fabricated and placed at the center of an arc motorized track (with a radius of 2 m). Two horn antennas have been mounted on the curved track. One of the horn antennas acts as an EM wave source to illuminate an oblique incident plane wave onto the surface of the reconfigurable retroreflector. The TE- and TM-polarized waves can be generated by rotating the antenna. Another horn antenna moves along the arc trajectory as a receiver to measure the scattered field at different angles.

Figures 6(a) and 6(b) show the fabricated metagrating-based retroreflector and the experimental setup. When the EM wave

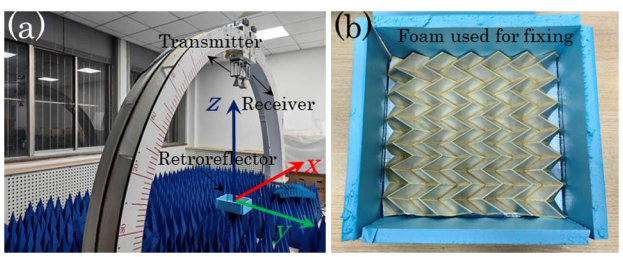

Fig. 6. (a) The image shows the arch test platform. (b) Sample picture of the origami retroreflector.

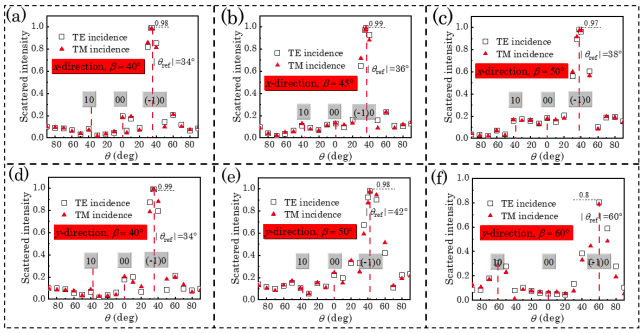

Fig. 7. When the wave vector is along the *x*-direction, experimental results of the scattered intensity distribution for retroreflection at various incidence angles of (a) 34°, (d) 36°, and (e) 38° under TE- and TM-polarized incidences. When the wave vector direction is along the *y*-direction, experimental results of the scattered intensity distribution for retroreflection at various incidence angles of (a) 34°, (d) 42°, and (e) 60° under TE- and TM-polarized incidences.

vector direction is incident along the *x*-direction, Figs. 7(a)–7(c) show the experimental results of reflection intensity for different retroreflection angles (34°, 36°, and 38°). When the wave vector direction is incident along the *y*-direction, Figs. 7(d)–7(f) show the experimental results of reflection intensity for different retroreflection angles (34°, 42°, and 60°). The reflection spectrum represents the reflection coefficients in different directions, thus accurately describing the efficiency of the retroreflector. The peak value of the reflected field intensity is normalized to the field intensity of the specular reflection, obtained by measuring the specular reflection intensity of an ordinary metal plate at the same incident angle. The red dashed line in each figure shows the reflection angle, where the incident wave is reflected in the same direction. In all cases, the experimental results agree with the simulation results.

4. Conclusion

In summary, we have designed an origami metagrating spin-locking retroreflector with a subwavelength scale ($f = 5$ GHz) through theory, simulation, and experiments. To achieve spin-locking, 2D metagrating that is insensitive to linear polarization must be employed. In addition, spin-locked retroreflection of CP waves over a range of continuous incidence angles can be achieved by continuously mechanically adjusting the folded state of the reconfigurable mirror. Compared with the traditional gradient metasurface-based retroreflector, the reconfigurable retroreflector has the advantages of low structure complexity, lightweight, high efficiency, and extensive adjustable range. We believe that the design of the origami 2D metagrating will open up new research avenues for manipulating CP wave extremes.

Acknowledgements

This work was supported by the National Natural Science Foundation of China (Nos. 61971437, 61971341, and

61971435) and the National Key Research and Development Program of China (No. 2022YFB3806200).

References

1. Y. Fu, J. Li, Y. Xie, *et al.*, "Compact acoustic retroreflector based on a mirrored Luneburg lensPhys," Rev. Mater. **2**, 105202 (2018).
2. H. D. Eckhardt, "Correction to: simple model of corner reflector phenomena," Appl. Opt. **10**, 2547 (1971).
3. J. J. Snyder, "Paraxial ray analysis of a cat's-eye retroreflector," Appl. Opt. **14**, 1825 (1975).
4. E. Sharp and M. Diab, "Van Atta reflector array," IRE Trans. Antennas Propag. **8**, 436 (1960).
5. W.-J. Tseng, S.-B. Chung, and K. Chang, "A planar van atta array reflector with retrodirectivity in both e-plane and h-plane," IEEE Trans. Antennas Propag. **48**, 173 (2000).
6. P. Ang and G. V. Eleftheriades, "A passive redirecting van atta-type reflector," IEEE Antennas Wireless Propag. Lett. **17**, 689 (2018).
7. M. Deng, T. Ren, J. Wang, *et al.*, "Doublet achromatic metalens for broadband optical retroreflector," Chin. Opt. Lett. **19**, 023601 (2021).
8. J. Ning, Y. Zheng, S. Wang, *et al.*, "Reconfigurable tri-mode metasurface for broadband low observation, wide-range tracing, and backscatter communication," Adv. Sci. **11**, 2304879 (2024).
9. A. Pesarakloo and M. Khalaj-amirhosseini, "Planar, wide-band omnidirectional retroreflector using metal-only transmit array structure for TE and TM polarizations," Sci. Rep. **12**, 11279 (2022).
10. Y. Jia, J. Wang, J. Yang, *et al.*, "Wideband planar retro-reflective metasurfaces for backscattering enhancement under oblique incidence," J. Phys. D **51**, 335103 (2018).
11. W. Yang, K. Chen, Y. Zheng, *et al.*, "Angular-adaptive reconfigurable spin-locked metasurface retroreflector," Adv. Sci. **8**, 2100885 (2021).
12. S. Sun, K. Yang, C. Wang, *et al.*, "High-efficiency broadband anomalous reflection by gradient meta-surfaces," Nano Lett. **12**, 6223 (2012).
13. A. Díaz-Rubio, V. S. Asadchy, A. Elsakka, *et al.*, "From the generalized reflection law to the realization of perfect anomalous reflectors," Sci. Adv. **3**, e1602714 (2017).
14. N. Mohammadi Estakhri and A. Alù, "Wave-front transformation with gradient metasurfaces," Phys. Rev. X **6**, 41008 (2016).
15. V. S. Asadchy, M. Albooyeh, S. N. Tcvetkova, *et al.*, "Perfect control of reflection and refraction using spatially dispersive metasurfaces," Phys. Rev. B **94**, 75142 (2016).
16. V. S. Asadchy, A. Díaz-Rubio, S. N. Tcvetkova, *et al.*, "Flat engineered multichannel reflectors," Phys. Rev. X **7**, 031046 (2017).
17. M. Li, L. Jing, X. Lin, *et al.*, "Angular-adaptive spin-locked retroreflector based on reconfigurable magnetic metagrating," Adv. Opt. Mater. **7**, 1900151 (2019).
18. Y. Ra'di, D. L. Sounas, and A. Alù, "Metagratings: beyond the limits of graded metasurfaces for wave front control," Phys. Rev. Lett. **119**, 67404 (2017).
19. Z. Zhu, Z. Qin, H. Wang, *et al.*, "Switchable chiral mirror based on PIN diodes," Photon. Res. **11**, 1154 (2023).
20. Y. Li, J. Zhang, S. Qu, *et al.*, "Achieving wide-band linear-to-circular polarization conversion using ultra-thin bi-layered metasurfaces," J. Appl. Phys. **117**, 044501 (2015).
21. Z. Zhu, Y. Cheng, Y. Li, *et al.*, "Four-function metasurface based on a tri-band integrated meta-atom for full space control of circularly polarized waves," Opt. Express **29**, 42569 (2021).
22. A. K. Bhattacharyya, *Microwave Journal* (Wiley, 2006).
23. Y. Ra'di and A. Alù, "Reconfigurable metagratings," ACS Photonics **5**, 1779 (2018).
24. Z. Zhu, Y. Li, Z. Qin, *et al.*, "Miura origami based reconfigurable polarization converter for multifunctional control of electromagnetic waves," Photon. Res. **12**, 581 (2024).